

Bioinspiration & Biomimetics



PAPER

Tactile surface classification for limbed robots using a pressure sensitive robot skin

RECEIVED
20 March 2014

REVISED
10 July 2014

ACCEPTED FOR PUBLICATION
22 July 2014

PUBLISHED
DD MM 2014

Jacob J Shill^{1,3}, Emmanuel G Collins Jr^{1,3}, Eric Coyle⁴ and Jonathan Clark^{2,3}

¹ Center for Intelligent Systems, Control, and Robotics (CISCOR), USA

² Scansorial and Terrestrial Robotics and Integrated Design Lab (STRIDe), USA

³ Department of Mechanical Engineering, FAMU & FSU College of Engineering, Tallahassee, FL, USA

⁴ Department of Mechanical Engineering, Embry-Riddle Aeron University, Daytona Beach, FL, USA

E-mail: jjshill@my.fsu.edu, ecollins@eng.fsu.edu, coylee1@erau.edu and jeclark@fsu.edu

Keywords: terrain classification, proprioception, legged robots

Supplementary material for this article is available [online](#)

Abstract

This paper describes an approach to terrain identification based on pressure images generated through direct surface contact using a robot skin constructed around a high-resolution pressure sensing array. Terrain signatures for classification are formulated from the magnitude frequency responses of the pressure images. The initial experimental results for statically obtained images show that the approach yields classification accuracies >98%. The methodology is extended to accommodate the dynamic pressure images anticipated when a robot is walking or running. Experiments with a one-legged hopping robot yield similar identification accuracies \approx 99%. In addition, the accuracies are independent with respect to changing robot dynamics (i.e., when using different leg gaits). The paper further shows that the high-resolution capabilities of the sensor enables similarly textured surfaces to be distinguished. A correcting filter is developed to accommodate for failures or faults that inevitably occur within the sensing array with continued use. Experimental results show using the correcting filter can extend the effective operational lifespan of a high-resolution sensing array over 6x in the presence of sensor damage. The results presented suggest this methodology can be extended to autonomous field robots, providing a robot with crucial information about the environment that can be used to aid stable and efficient mobility over rough and varying terrains.

1. Introduction

The stability and operating efficiency of a running robot in part depends on the device's control strategy, leg gait, and operating environment. Previous research with legged robots has developed a variety of stable leg gaits [1–3]. A robot's performance can be heavily dependent on the type of terrain the robot is traversing [4–7]. The importance of using the proper leg gait on different terrains can be seen with humans when they transition from running on a concrete surface to a sandy surface. Unless the person changes their leg coordination (e.g. leg gait), their running performance will decrease, and the person can even experience instability, e.g., fall over [8, 9]. As a result of terrain dependence, it is important to develop methodologies that enable a limbed robot to recognize new terrain surfaces as they are encountered.

Terrain surface classification can, of course, be accomplished using vision. Vision-based classification techniques have been developed for wheeled robots [10–14] and are expected to be extendable to legged robots. However, proprioception is needed to complement vision for at least the following reasons: (1) a robot's vision may be focused away from the terrain; (2) vision may fail or be unreliable due to lack of lighting, ambient smoke, or fog; (3) superficial ground debris (e.g., leaves) may obscure the underlying surface (e.g., mud); (4) vision may fail due to sensor malfunction.

Proprioceptive terrain classification has been accomplished on wheeled robots and electric powered wheelchairs primarily by using vibration sensors [15–17]. For AQUA, a RHex-type legged robot, proprioceptive classification has been performed by combining robotic states at prescribed leg angles, six-axis IMU

measurements, and leg motor driving currents [18]. More recently, the leg motor currents in conjunction with dynamic models for the X-RHex Lite (XRL) robot have been used to achieve surface identification [19]. However, a common limitation of these proprioceptive classification methods is that the measured terrain signatures used for identification are coupled to the vehicles dynamics, which depends on operating conditions such as speed and payload. (This is discussed in some detail for wheeled robots in [17, 20].) As a consequence, robust terrain classification requires training on a wide variety of operating conditions. This approach is a time consuming process and can dramatically increase a classifier's computation time.

This paper presents a new approach to proprioceptive terrain identification; in particular, motivated by biological skin which cognitively implements pressure reactions from densely-spaced nerves. The described method, which is designed with an emphasis for use with limbed robots, is largely independent of the vehicles dynamics. Terrain signatures are to be measured using a piezoelectric pressure sensors that intermittently come into direct contact with the surface.

First, an artificial skin composed of layers which replicate mechanical properties of human skin, and in addition protect an embedded high-resolution pressure sensing array. The sensor is intended provide the same functionality as the densely-spaced nerves in human skin, the basis for the sensation of touch. This covering is called pressure sensitive robot skin (PreSRS, pronounced 'pressures'). A classification methodology is then developed using the magnitude spatial frequency response of the pressure images obtained from PreSRS; the methodology can apply to pressure images derived from any robot skin yielding uniformly spaced pressure measurements. The initial experiments display classification accuracies >98% for static measurements, which can be analogous to measurements taken when a robot is standing still. Further experiments apply PreSRS to a one-legged hopping robot and show that by properly sampling the dynamic pressure images, similar classification accuracies can also be achieved.

Additionally, this paper explores the importance of using high-resolution pressure images for terrain classification. Particularly, it describes experiments demonstrating that high-resolution is necessary when seeking to distinguish similarly textured surfaces or redundancy for when sensors in the sensing array inevitably fail.

It is important to note that although the focus of this research is terrain surface sensing using the feet of limbed robots, the basic methodology can also be used to enable the end effector of a manipulator to sense a surface.

The paper is organized as follows: section 2 reviews the use of proprioceptive sensing with manipulator

end effectors for object and surface classification. Section 3 details the methodology and biological inspiration used in the construction of PreSRS, the robot skin used in this research. Section 4 describes a terrain classification approach based on pressure images and uses PreSRS to classify four common terrain surfaces under a static load. Section 5 provides insight into one of the reasons a high-resolution sensor array is essential for surface classification; it enables distinguishing between similar surfaces. Section 6 describes the integration of PreSRS onto the foot of a one legged hopping robot. Section 7 shows how the terrain classification approach of section 4 can be extended to dynamic pressure images and presents the results of dynamic terrain surface classification experiments with the one-legged hopper. The results provide strong evidence that the PreSRS based classification approach is not dependent upon the vehicle operating condition. Section 8 also considers the use of PreSRS on the hopper and presents a method to repair the pressure images corresponding to damage to the pressure sensing array. Finally, section 9 presents conclusions and future work.

2. Background

For manipulators proprioceptive surface classification and object recognition have previously been achieved by enhancing the end-effectors of the manipulators with tactile sensors [21–25]. These sensors are typically capacitance or piezoelectric based sensing arrays, or vibrational sensors.

Piezoelectric type sensing arrays are grids composed of individual strain gauge circuits, whereas capacitance type sensing arrays consist of cells with two electrically charged materials separated with an insulator. Applying pressure to either sensing array type produces an electrical signal proportional to the applied pressure. The fingers and palm of the commercially available BarrettHand[®] are fitted with high-resolution capacitance based pressure sensing arrays from Pressure Profile Systems, Inc., with 162 individual pressure-sensing cells [26].

Proprioceptive object recognition has been achieved using piezoelectric type pressure sensing arrays mounted on an end effector. This was achieved by pressing the sensing area against an object such as a screw or washer, which creates a pressure image that can be used with simple pattern recognition techniques to identify the object [21, 22]. A more complex 3D image of the object has been constructed by using a planned path to explore the object and with pattern recognition type calculations [23, 27].

Efforts to use proprioceptive sensors to classify surfaces include the development of a bio-inspired artificial finger nail equipped with a single three-axis accelerometer for a humanoid robots. Here surfaces were identified based on the vibrations and auditory

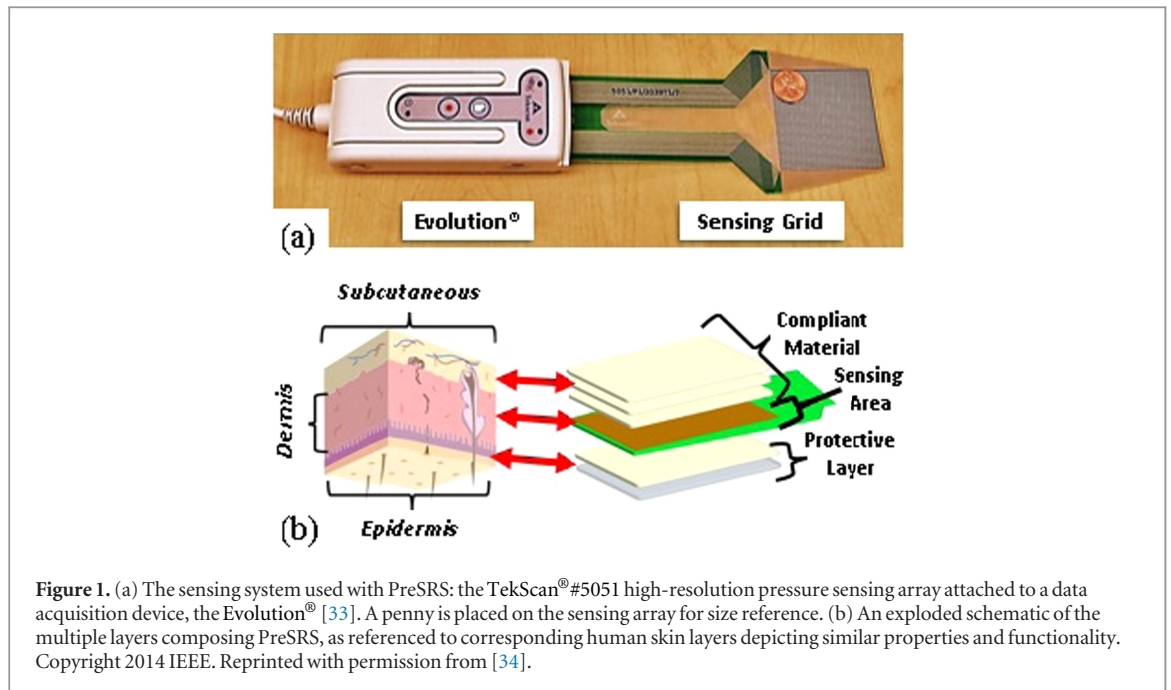


Figure 1. (a) The sensing system used with PreSRS: the TekScan® #5051 high-resolution pressure sensing array attached to a data acquisition device, the Evolution® [33]. A penny is placed on the sensing array for size reference. (b) An exploded schematic of the multiple layers composing PreSRS, as referenced to corresponding human skin layers depicting similar properties and functionality. Copyright 2014 IEEE. Reprinted with permission from [34].

feedback measured when the finger was dragged across a textured surface [24, 28]. This method identified 20 different textured surfaces with an 80.0% accuracy. Another study constructed a bio-inspired artificial finger with multiple embedded accelerometers to capture vibrational signatures when sliding the finger over textured surfaces [25, 29]. The study classified 117 different surfaces at 99.6% accuracy, in addition to measuring the surface compliance.

For end effectors it makes sense to prescribe delicate motions and measure vibrations for surface classification, however the large impacts associated with running make this approach problematic. Hence, a new technique is developed using a high-resolution pressure sensing array embedded in a robotic foot.

3. Constructing a pressure sensitive robot skin

Nerve ending clusters respond to static and dynamic skin deformation events by sending the form, texture, location, and/or pressure intensity information of the contacting surface to the brain [30]. Touch is mediated in human feet through skin using four types of nerve receptors, named *Merkel*, *Ruffini*, *Pacini*, and *Meissner* [31]. These qualities of human skin inspired the implementation of a high-resolution sensing array during the development of PreSRS.

Merkel nerves are the most common nerves in the skin of human hands, and can detect the static deformation of shapes, edges, and rough textures. The Ruffini nerves, located deep in the skin, are oriented parallel to skin stretch lines allowing responses to shear stress inflicted of the skin. Pacini nerves are found in the subcutaneous layer and respond to high frequency (250–350 Hz) vibrations induced on the

skin. These nerves play an important role in detecting fine surface textures. Merkel nerves are found in the epidermis, and respond to relatively low-frequency vibrations (30–50 Hz) that can occur when textured objects are moved across the skin [32].

The TekScan® #5051 high-resolution sensor, shown in figure 1(a), consists of 1936 individual piezoelectric based strain gauges, evenly arranged to form a 44 sensor \times 44 sensor grid. The individual sensors are most like the Merkel nerve endings, which are most common in hands and sense normal deformations. The array effectively measures pressure distributions across a 55.88 mm \times 55.88 mm area within a 0–138 kPa range. There are small drifts in the sensor measurements due to the underlying piezoelectric elements. However, the experiments conducted as a part of this research indicate that these changes do not affect the classification accuracy.

The sensor readings are correlated to pressure intensities in eight-bit integer format, sampled at 100 Hz, using the Evolution® acquisition device, displayed in figure 1(a) attached to the #5051 sensor [33]. Individual measurements are kept in eight-bit integer format and are saved as 44 pixel \times 44 pixel images \mathbf{I} , where the $\mathbf{I}(i, j)$ pixel refers the individual sensor with matching grid indexes (i, j) .

Figure 1(b) shows the three layers making up human skin: the (inner) *subcutaneous* layer, the (middle) *dermis* layer, and the (outer) *epidermis* layer.

As illustrated in figure 1(b), the subcutaneous and epidermis skin layers are emulated using sheets of a compliant material (each \sim 3.0 mm thick). Human skin is a non-homogenous viscoelastic material, possessing mechanical properties that vary between individuals and skin location [35, 36]. The subcutaneous layer has the desired property of conforming the skin

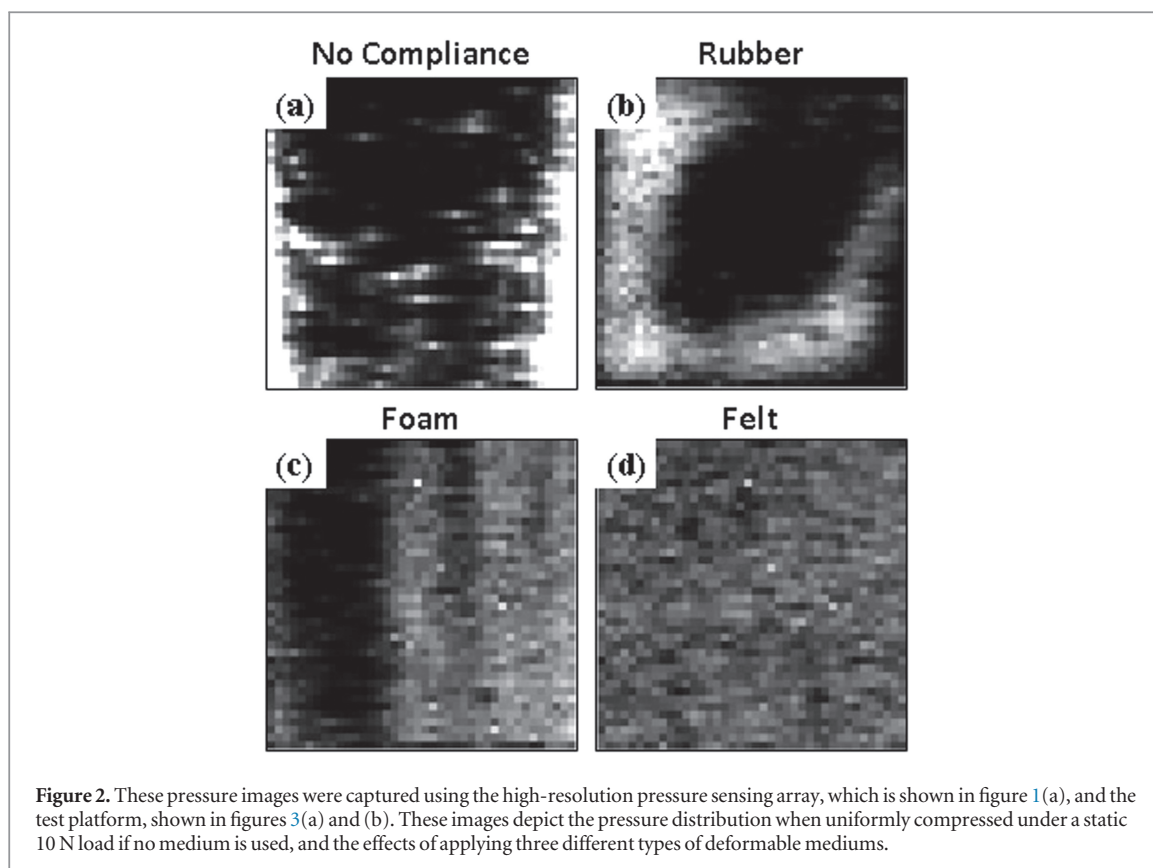


Figure 2. These pressure images were captured using the high-resolution pressure sensing array, which is shown in figure 1(a), and the test platform, shown in figures 3(a) and (b). These images depict the pressure distribution when uniformly compressed under a static 10 N load if no medium is used, and the effects of applying three different types of deformable mediums.

to surfaces, allowing many nerve endings to make contact. Hence, the substitute material should produce a pressure image in which all the individual pixels have similar intensities (e.g., low standard deviations) when the sensor is compressed with uniform static load. A suitable substitute was chosen by experimenting with several types of elastically deformable materials (see figure 2).

PreSRS was initially used to sense the surface of a variety of materials using the test platform shown in figures 3(a) and (b), which is described in further detail in section 4.1. The platform presses the sensing array and test material between two flat aluminum plates with an evenly dispersed 10 N static load. Pressure images obtained from these tests are displayed in figure 2 as grayscale images. The white image pixels of figure 2 correspond to the sensor and surface making contact, where brighter pixels reflect greater pressure magnitudes. The dark regions represent the absence of contact between the sensor and surface.

With no compliant material, as seen in figure 2(a), the image intensity is concentrated along the perimeter of the sensing array. This uneven measured load distribution is caused by the imperfect flatness of the two contacting surfaces. Super-soft neoprene rubber failed to produce the desired even-intensity pressure image, due to the fact that rubber, an incompressible substance, deflects by changing shape rather than changing volume [37]. Hence, when compressed with the sensor, rubber strains/stretches the sensor circuits, which propagates the load measurement along

discrete regions of the sensing array. The resulting distorted pressure image is displayed in figure 2(b). The foam material, as seen in figure 2(c), performed better than rubber, however it did not yield an even-intensity image.

The pressure image in figure 2(d) reveals that a felt type fabric is a better skin substitute since it yields the desired, evenly distributed, pressure image. The fabric chosen is made up of 35% wool and 65% viscose rayon, which are ‘felted’ together into ~ 3.0 mm thick sheets. The fibers have a combined density of 1.45 g cm^{-3} [38], and the fabric density is 0.0197 g cm^{-3} . Based on the ratio of fiber to fabric density, felt is essentially ($\approx 99\%$) composed of empty space. This gives the material excellent compressive properties and, as seen in figure 2(d), the strain effects associated with both rubber and foam materials are non-existent.

Figure 1(b), shows the high-resolution pressure sensing array correlating to the dermis layer of human skin, which contains the nerve endings essential to biological touch. The sensor pitch value of 1.27 mm (i.e., the distance between sensors) closely matches human nerve pitch (i.e., the distance between nerves), which can be approximately 1.00 mm in finger tips [39].

The protective nature of the epidermal human skin layer was replicated with a hard silicon-rubber covering (>1.0 mm thick), as shown in figure 1(b). The silicon-rubber material has a high stiffness, therefore it deforms negligibly under compression and is resistant to puncture damage.

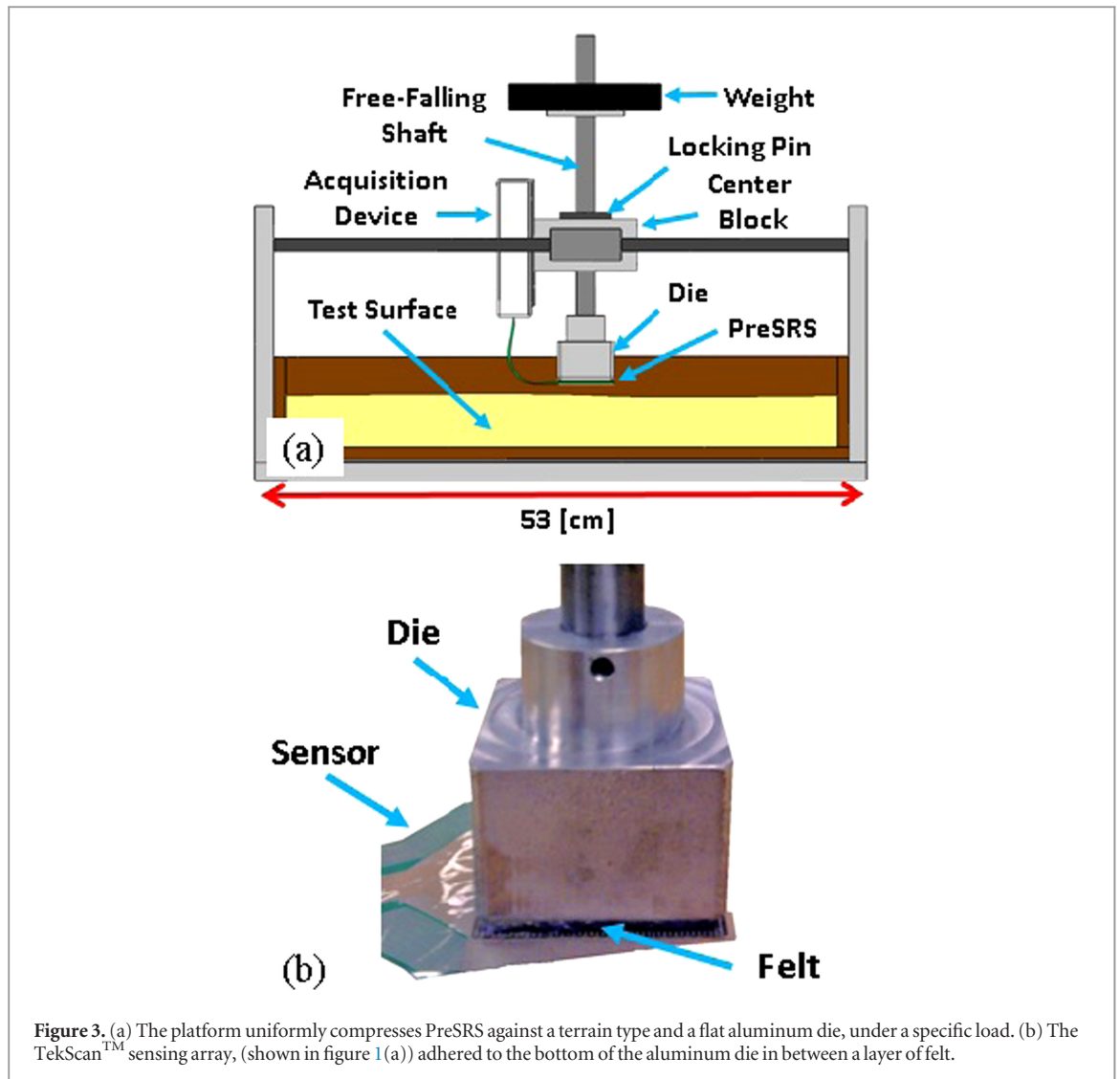


Figure 3. (a) The platform uniformly compresses PreSRS against a terrain type and a flat aluminum die, under a specific load. (b) The TekScan™ sensing array, (shown in figure 1(a)) adhered to the bottom of the aluminum die in between a layer of felt.

The PreSRS layers were adhered together with 3M™ super 77 spray adhesive, making PreSRS approximately 10 mm thick.

4. Static terrain classification using preSRS

This section describes an experiment used to classify terrain signatures captured with PreSRS under static conditions. The experiment, analogous to terrain classification by a limbed robot standing in a stationary position, was used to validate the basic methodology of implementing high-resolution pressure images for surface identification purposes. Section 4.1 describes the procedure used to collect terrain samples. Section 4.2 details the methodology used to train a classifier using pressure images and presents the classification accuracy achieved.

4.1. Terrain samples

Using a high-resolution pressure sensing array to capture terrain signatures on a robot foot for classification purposes had not previously been demonstrated in the literature. Therefore, before integrating PreSRS

with a robot, a characterization experiment was conducted on four common terrain types.

The test platform, illustrated in figure 3(a), was used to capture static pressure images with PreSRS against a variety of terrain types. PreSRS was attached to a flat polished aluminum compression die using 3 M™ super 77 adhesive spray, as seen in figure 3(b). The die shaft, pinned to a center block, positioned the die approximately 5.0 mm above a terrain type. The center block is adjustable in order to reposition the die to a undisturbed terrain patch for each recorded image. The die side dimensions were intentionally made 5.08 mm less than the #5051 sensor side dimensions. This ensured the compressive load was distributed only on the sensing area. Individual trays with approximate dimensions 53 cm × 32 cm × 7 cm were used to house the terrains.

Terrain pressure images were collected individually by removing the pin holding the die shaft loaded with 10 N, which then free-falls roughly 5.0 mm until PreSRS impacts and remains on the terrain. The TekScan® software reads sensor data from the Evolution® acquisition device to a computer. To

ensure steady-state (e.g., static) measurements, the pressure image were recorded exactly 2.50 sec after impacting the surface, and then saved as eight-bit images \mathbf{I} .

The four common terrains used were: flat polished aluminum, dry beach sand, dry pine needles, and dolomite gravel (roughly 10 mm–50 mm in diameter). Implementing the compression test platform, seen in figure 3, 100 terrain samples were measured with PreSRS on each terrain type (400 total).

Pressure images were cropped, removing the outer two rows and columns. This made the sensing array and the die dimensions equal. The resulting 40 pixel \times 40 pixel images contain 1600 uniformly spaced sensors spanning a 50.8 mm \times 50.8 mm area. Examples of terrain pressure images captured in this experiment are displayed in the second column of figure 4. The fact that these pressure images can be visually distinguished, is strong evidence that a high-accuracy classifier can be developed.

4.2. Classification

It has been shown in [17, 40] that the magnitude frequency response of the spatial domain terrain sample constitutes signatures unique to the terrain type. Hence, it can be used to define feature vectors a classifier can train and identify.

The rows of the 2D pressure images \mathbf{I} are first aligned and padded with zeroes to obtain $\mathbf{X} \in \mathbb{R}^N$, such that

$$\mathbf{X} = \text{vec}(\mathbf{I}), \quad (1)$$

where $\text{vec}(\cdot)$ is the standard row aligning operator, and $N = 2048$. The fast Fourier transform is used to compute the (spatial) discrete Fourier transform $\mathbf{Y} \in \mathbb{C}^N$, given by

$$Y(k+1) = \sum_{\ell=0}^{N-1} X(\ell+1) e^{-j2\pi k\ell/N}, \quad k = 0, 1, \dots, N-1, \quad (2)$$

where $\mathbf{Y}(i)$ denotes the i th element of the vector \mathbf{Y} . Next, let $\mathbf{Z} \in \mathbb{R}^N$ denote the vector containing the magnitudes of the elements of \mathbf{Y} such that

$$\mathbf{Z}(i) = \text{abs}(\mathbf{Y}(i)), \quad i = 1, 2, \dots, N. \quad (3)$$

Since the elements of \mathbf{Z} are mirrored, only the first half of the elements are placed in a feature vector $\mathbf{F} \in \mathbb{R}^n$, where $n = N/2 + 1 = 1025$.

Figure 5 provides the magnitude frequency response feature vectors \mathbf{F} computed from the pressure images \mathbf{I} that are shown in figure 4. The plots depict the frequency range where the magnitude spikes are most significant, the full frequency range spans 2032 cycle mm^{-1} . A key characteristic shared by the feature vectors in figure 5 is that the magnitude spikes occur at the same frequencies (50.8 cycle mm^{-1}) but at different intensities per terrain type. The spike frequency intervals are an artifact of the

piecewise row aligning operation of (1). Spike magnitude differences between terrain types create distinguishing metrics for the classifier to exploit.

A Parzen windows estimation (PWE) classifier, which is described in [41] in the context of terrain classification, was trained using 20 randomly selected feature vectors \mathbf{F} per terrain type (80 total). The 20 feature vectors are split into two sets: 13 for a training set $\mathbf{T} \in \mathbb{R}^{p \times n}$, where $p = 52$, and 7 for a validation set $\mathbf{V} \in \mathbb{R}^{q \times n}$, where $q = 28$.

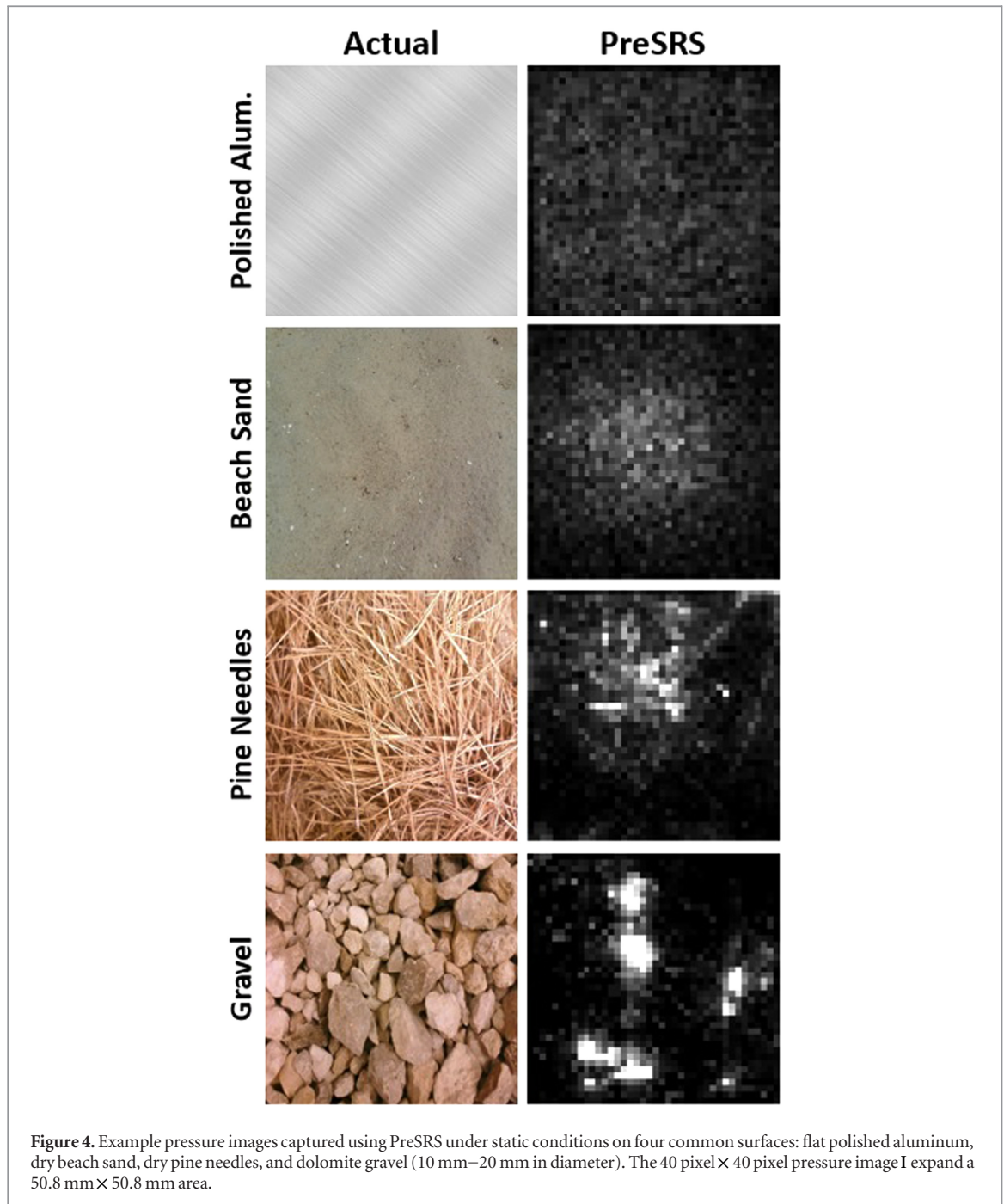
Principal component analysis (PCA) was implemented in training to determine a reduced feature space h ; this process is discussed in [41]. Using PCA to train the PWE classifier reduces the feature dimensions from $n = 1025$ to $h = 52$, which dramatically decreases dimensionality and optimizes accuracy. Terrain identification computation times are approximately 0.245 msec when using a 2.67 GHz Intel® Core™2 Duo CPU.

Training produces the transformation matrix $\mathbf{U} \in \mathbb{R}^{h \times n}$, for reducing the input feature vector space, and matrix $\mathbf{P} \in \mathbb{R}^{h \times (p+q)}$ with columns correlating the reduced order feature space from PCA. The trained PWE was used to identify the remaining 80 feature vectors per terrain type (320 total). These terrain samples were not used in the training process. Classification was performed by first computing the corresponding terrain sample feature vector $\mathbf{F} \in \mathbb{R}^n$ and then obtaining the reduced order feature vector $\mathbf{Q} \in \mathbb{R}^h$ using $\mathbf{Q} = \mathbf{U}\mathbf{F}$. PWE compares \mathbf{Q} with the columns of \mathbf{P} and provides the terrain type probabilistically most associated with the sample.

Table 1 shows the terrain classification results obtained with the trained PWE classifier when identifying the 320 pressure images captured using PreSRS. 100% accuracies were achieved when classifying flat polished aluminum, dry beach sand, and dolomite gravel. One tested pressure image was misclassified as dry beach sand instead of dry pine needles. Hence, 319 out of 320 (99.7%) terrain pressure images were successfully classified with the PWE classifier. These results clearly demonstrate the basic capacity of PreSRS with a PWE classifier for attaining reliable terrain classification in a static environment.

5. Resolution experiment

The high classification accuracy achieved in section 4 on four distinct terrains raises two relevant questions: how fine of a distinction between surfaces can the classification approach accurately distinguish, and how important is the high-resolution component of PreSRS to classification? This section presents experimental results indicating the need for high-resolution sensing when distinguishing similar surfaces. Additionally, results are presented that characterize the classification performance of both low and high-



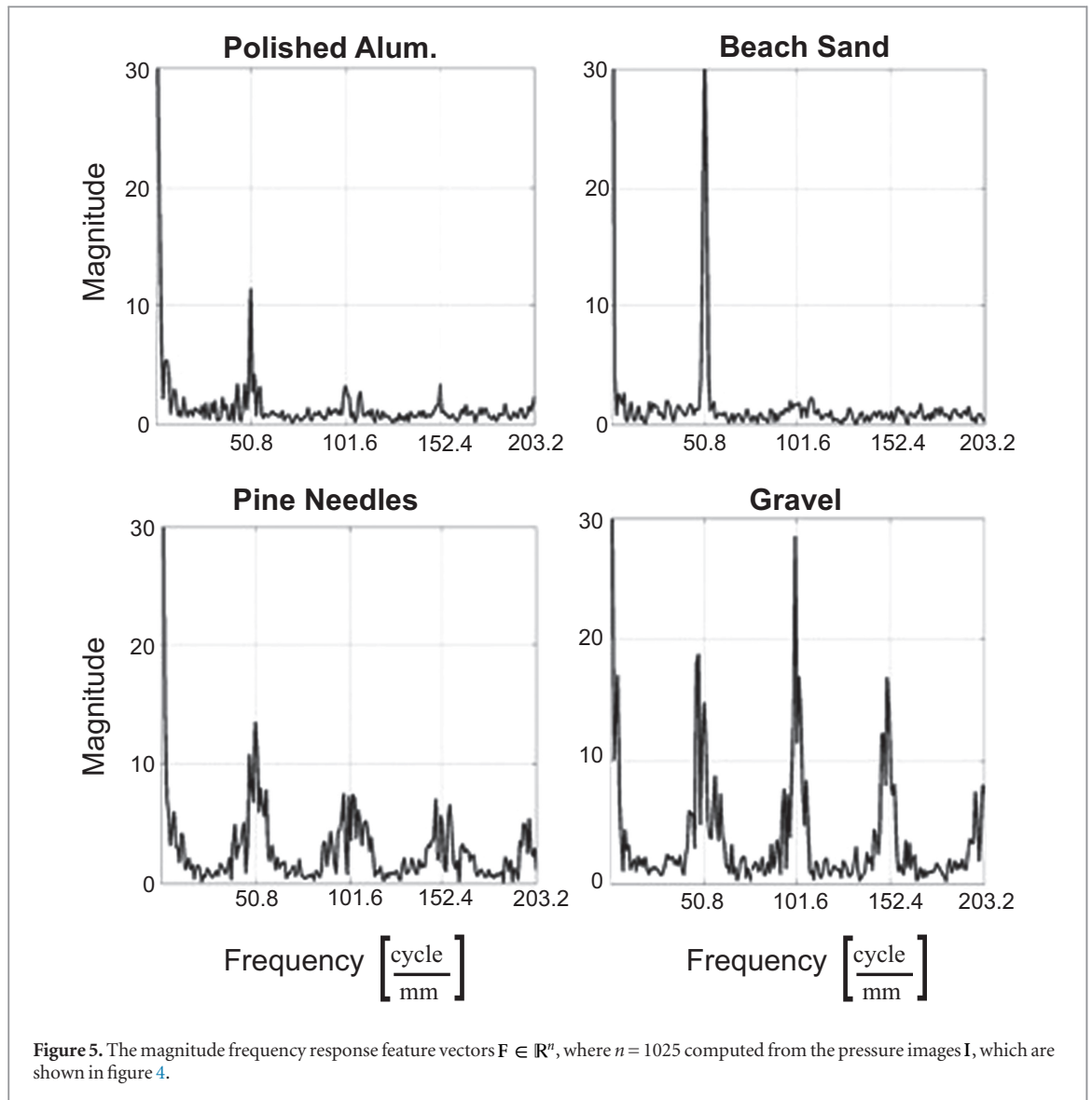
resolution sensing arrays on similar and distinct terrains.

A surface classification experiment, similar to the one performed in section 4, was conducted on five similarly textured surfaces: flat polished aluminum, and four sequentially rougher grades of sandpaper: 220 grit, 150 grit, 100 grit, and 60 grit. The sandpaper is composed of aluminum oxide particles adhered to a fabric backing. Table 2 was generated from the sandpaper technical specifications [42], and reveals how the aluminum oxide particle diameters increase with each decreasing grit number.

Using PreSRS, 50 pressure images per surface were statically captured under a 10 N load using the test

platform shown in figure 3. For testing purposes, low-resolution pressure images were simulated by increasing the sensor pitch from 1.27 mm to 5.59 mm. Figure 6 outlines this transformation process, which extracts every fourth image pixel (by both row and column) from the high-resolution image. This creates a 10 pixel \times 10 pixel image containing 100 individual sensors, 1500 less than the high-resolution image. The low-resolution images cover the same spatial domain area as the high-resolution images.

For each sandpaper grit number, figure 7 displays both the low and high-resolution pressure images adjacent to each other, while the flat polished aluminum image is shown in figure 6. Both sensor

**Table 1.** Static results.

Detected	Actual			
	Pol. alum.	Sand	Pine ned.	Gravel
Pol. alum.	100%	–	–	–
Sand	–	100%	1.30%	–
Pine ned.	–	–	98.7%	–
Gravel	–	–	–	100%
Overall accuracy = 99.7%				

Table 2. Sandpaper specifications.

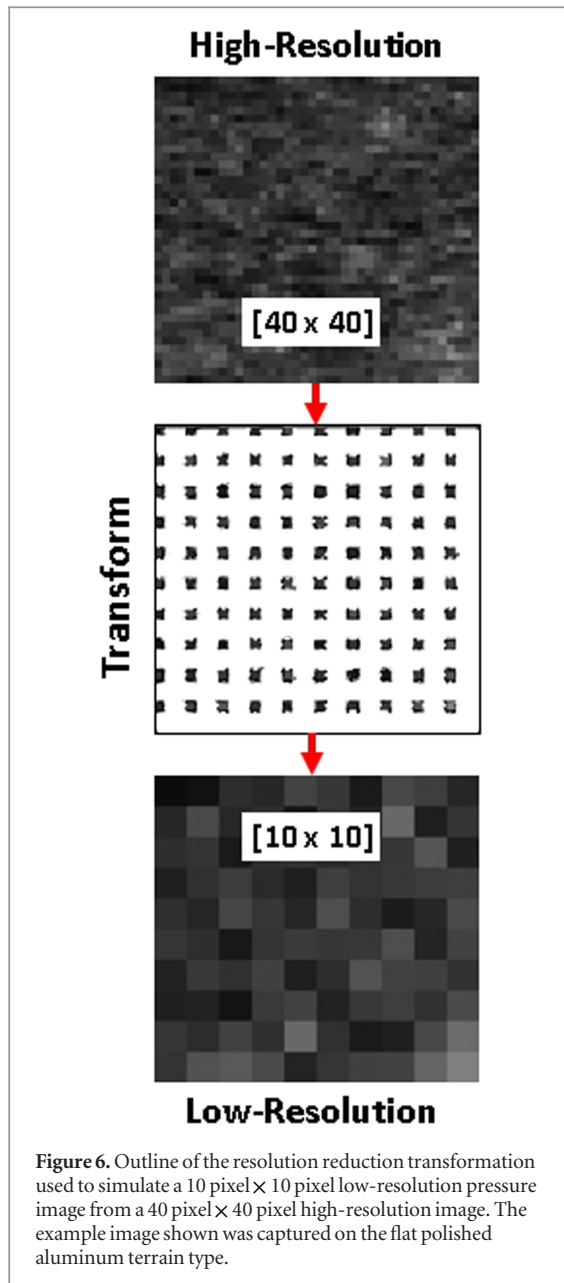
Grit no.	Particle dia.
220	58 μm
150	82 μm
100	129 μm
60	260 μm

resolutions produce pressure images that are not visually distinguishable. This is not surprising due to the fact the sandpaper surfaces are very difficult to distinguish via human touch. However, it is clearly evident that the high-resolution images contain much more detail.

Magnitude frequency response feature vectors were calculated using the pressure images using the method outlined in section 4. Example feature vector signatures for the two extreme textured surfaces,

polished aluminum and 60 Grit sandpaper are shown in figure 8. Although, the signatures in figure 7 do not have distinguishing attributes between terrain types, the high-resolution feature vector $\mathbf{F} \in \mathbb{R}^{1025}$ contains far greater detail than the low-resolution vector $\mathbf{F} \in \mathbb{R}^{65}$. Each sensor resolution type covers the same spatial domain area of 50.8 mm \times 50.8 mm.

Following the classification methodology outlined in section 4, two PWE classifiers, one per resolution, were trained with 20 randomly selected feature vectors per terrain (100 total). Using these trained classifiers, the remaining feature vectors (30 per terrain type) were identified.



Even though both the spatial and frequency domains of the high-resolution PreSRS images show little discrepancies, the PWE classifier produced an overall classification accuracy of 96.7%. The surface classification accuracy of the simulated low-resolution PreSRS images had a low accuracy of 58.0%. These results indicate a high-resolution sensing array, like the TekScan[®] #5051 sensor, is needed to distinguish between very similar surfaces.

Another experiment was performed using the pressure images collected in section 4, where the four tested dissimilar terrains (polished aluminum, sand, pine needles, and gravel) samples were reduced to 10 pixel \times 10 pixel images (not shown in this paper). A PWE classifier was trained and tested in the same matter, resulting in an overall classification accuracy of 98.8%.

Thus a low-resolution sensing array can produce high terrain classification accuracies if the terrain types are sufficiently distinct.

6. Integrating presrs with a one-lagged hopping robot

PreSRS was intended to be used on robotic feet, where the pressure images will be measured dynamically while the robot is walking or running. This section describes the FAMU-FSU hopper and the robot foot designed to accommodate PreSRS; which allowed for the transition from using static pressure images to using dynamic pressure images for terrain classification.

Figure 9(a) displays the FAMU-FSU hopper, which can be modeled as a spring loaded-inverted pendulum (SLIP) type runner. The robot is attached to a boom (1.4 m in length), constraining forward motion to a circular track. The robot has two operating phases, as illustrated in figure 9(b): a stance phase, where the hopper is in contact with a surface, and a flight phase [43].

Robot control during a stance phase uses an active energy removal (AER) protocol that changes the hopper leg length during a stance as described by

$$\zeta(t) = \zeta_o - \zeta_{dev} \sin(\omega t + \phi), \quad (4)$$

where ζ_o corresponds to the robot rest leg length, ζ_{dev} depicts the amplitude of recirculation, and the two control parameters ω and ϕ set the desired frequency and phase of recirculation respectfully. The AER protocol was designed to allow the hopper to robustly run over large obstacles (up to 20% of the hopper leg length) [4].

During flight phase, the controller sets the next robot leg touchdown angle β_{n+1}^{TD} using the governing equation

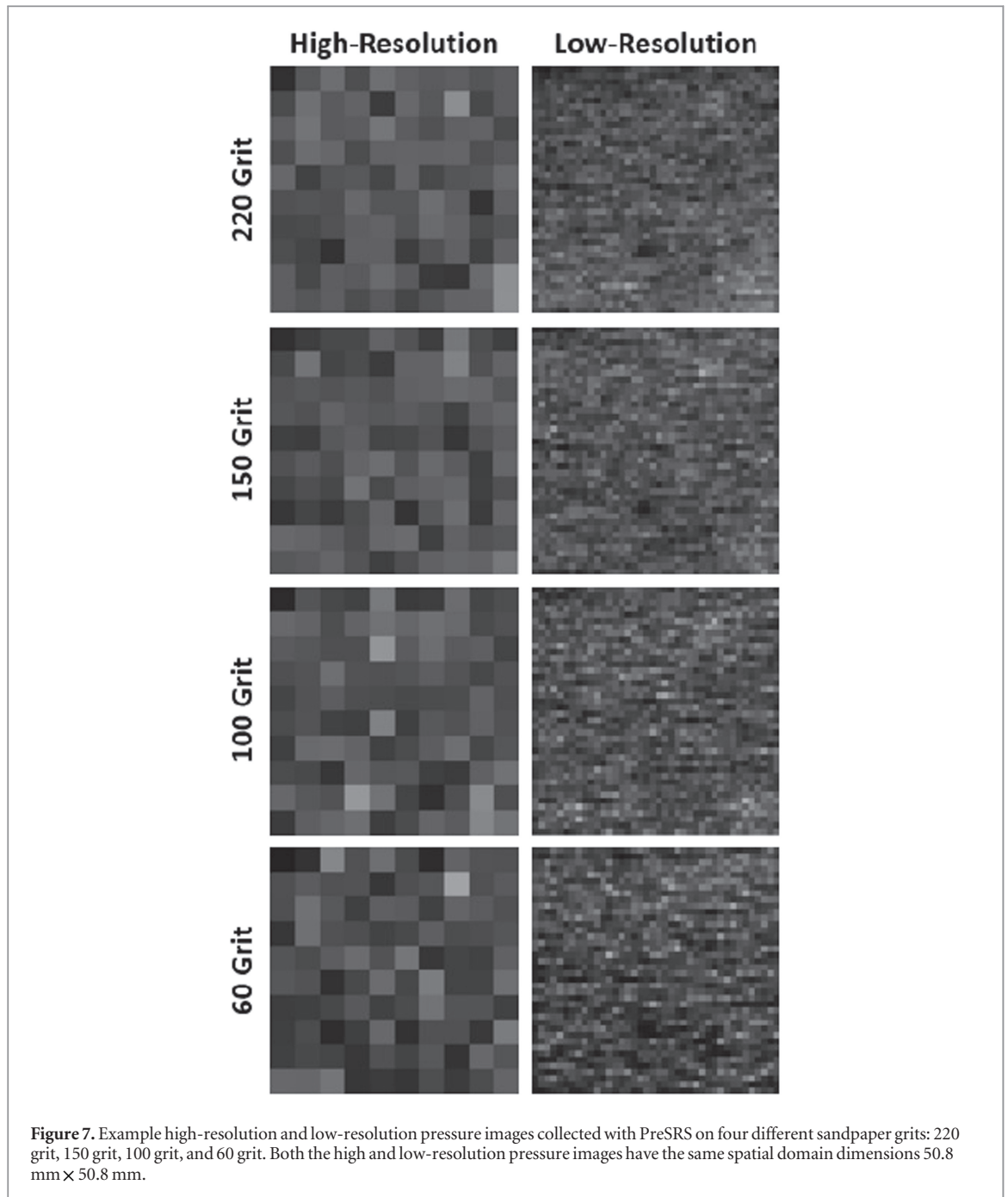
$$\beta_{n+1}^{TD} = \beta_n^{LO} + c(\beta_n^{TD} - \beta_{des}^{TD}), \quad (5)$$

where β_n^{TD} is the previous leg touchdown angle, β_n^{LO} is the previous leg liftoff angle, c is a weighted parameter, and β_{des}^{TD} is the desired touchdown angle.

The four control parameters ω , ϕ , c , and β_{des}^{TD} mandate leg gaits $G_i(\omega, \phi, c, \beta_{des}^{TD})$. Parameters ϕ and c are stabilizing factors, and parameters ω and β_{des}^{TD} control the robot forward velocity and hop height [4, 43].

The surface area of the original hopper foot was too small to attach PreSRS, which has a 55.88 mm \times 55.88 mm sensing area. Hence, a new hopper foot was designed to have an elliptical aluminum base having a 48.3 mm \times 52.1 mm cross-sectional area, as illustrated in figure 10.

This new robot foot ensures high quality pressure images by taking design cues from human ankle biology. The human ankle allows the foot to remain stationary relative to the ground during a step and by

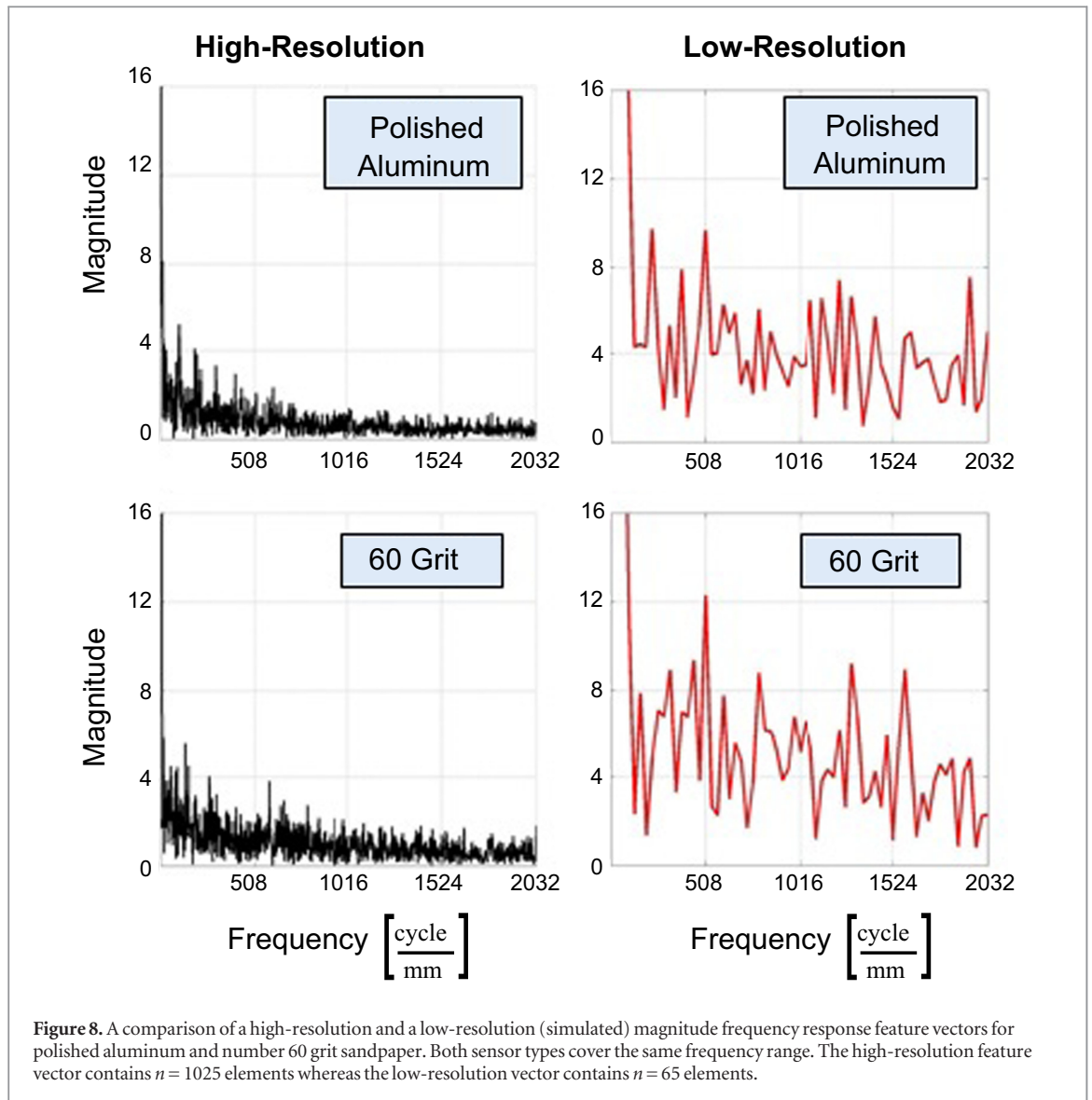


compressing the viscoelastic adipose tissue beneath the heel, dissipates energy and shock conforming the skin to the contacting surface [44, 45].

These biological qualities are replicated with a mechanically compliant ball joint connection between the hopper leg and foot, which is constrained with the compression spring of figure 10. The connection allows the foot to pitch, yaw, and roll as the robot leg progresses through a step. The compliant layers composing PreSRS, shown in figure 1(b), both absorb impact shock and maximize the contact area between the high-resolution pressure array and the terrain.

Additionally during a step period, the ball joint activates a micro switch embedded in the foot, seen in figure 10, initiating the AER control protocol. When the robot enters a flight phase, the micro switch in the foot deactivates, and the leg recirculation controller becomes active.

Figure 11 illustrates the dynamics of this new robot foot with high-speed frame shots taken throughout a step. As seen in figure 11, the foot base flattens, conforming to the surface. The foot remains stationary relative to the ground over the entirety of the step period, as the robot leg pivots about the ball joint connection from touchdown angle β_n^{TD} to liftoff angle β_n^{LO} .



7. Terrain classification using dynamic pressure images

The terrain classification experiment outlined in this section uses dynamic pressure images captured using PreSRS on the FAMU-FSU hopper. Section 7.1, details the experimental procedure instituted when collecting terrain data. Section 7.2, discusses the identification methodology implemented and presents the resulting classification accuracies.

7.1. Experimental procedure

Previous terrain classification techniques that use data influenced by the robot dynamics have shown to be effective (achieving accuracies above 90%), so long as the robot operates in the same manner (i.e., leg gait G_i) used to train the classifier [17–19]. Changing operating modes, however, changes the dynamic behavior of the robot, which changes the terrain sensor data. Hence, for these systems classifiers have to be trained with data from multiple operating conditions.

A key motivation for developing PreSRS was to accurately identify terrains regardless of the system operating conditions. Hence, PreSRS was designed to capture terrain features through direct contact and not via the robot dynamics. Therefore, a classifier trained with pressure images associated with hopper leg gait G_i should accurately identify terrain samples collected from gait G_j , where $i \neq j$.

It follows from the discussion in section 6, that for fixed stabilizing factors ϕ and c , a hopper leg gait $G_i(\omega, \beta_{des}^{TD})$ can be defined with the two control parameters, ω and β_{des}^{TD} . Three distinct leg gaits were used in this experiment, $G_1(6.0 \text{ rad sec}^{-1}, 0.27 \text{ rad})$, $G_2(6.5 \text{ rad sec}^{-1}, 0.42 \text{ rad})$, and $G_3(7.0 \text{ rad sec}^{-1}, 0.57 \text{ rad})$; each successive gait differed by increasing the control parameters ω and β_{des}^{TD} .

Dynamic terrain pressure images were collected using the FAMU-FSU hopper and PreSRS on four common surface types: smooth pine wood planks, standard flooring carpet, semi-moist clay dirt, and thick Spanish style grass. The circular (2.8 m diameter)

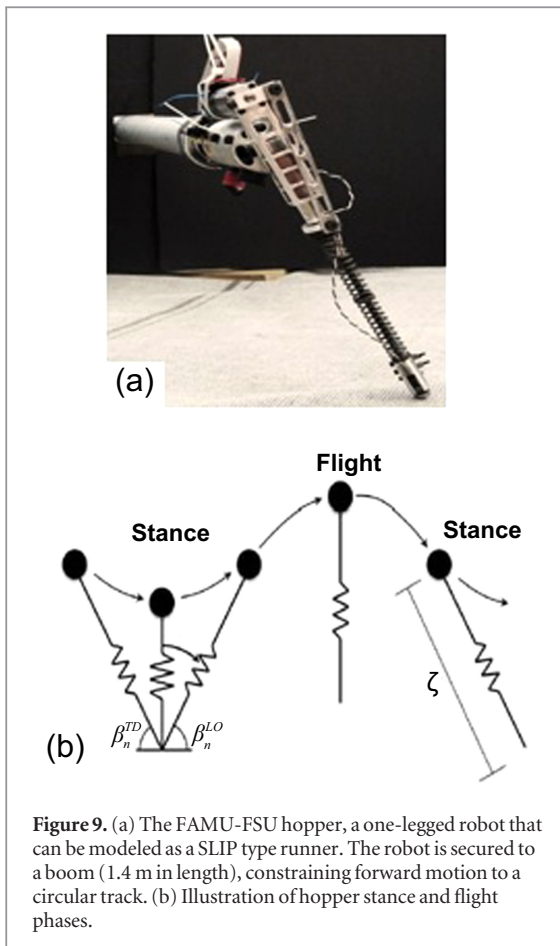


Figure 9. (a) The FAMU-FSU hopper, a one-legged robot that can be modeled as a SLIP type runner. The robot is secured to a boom (1.4 m in length), constraining forward motion to a circular track. (b) Illustration of hopper stance and flight phases.

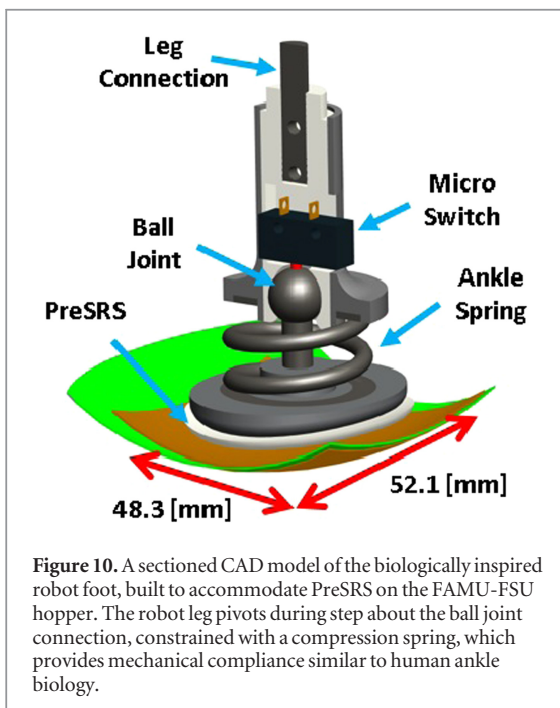


Figure 10. A sectioned CAD model of the biologically inspired robot foot, built to accommodate PreSRS on the FAMU-FSU hopper. The robot leg pivots during step about the ball joint connection, constrained with a compression spring, which provides mechanical compliance similar to human ankle biology.

track housed the terrains with barriers around the inside and outside perimeter. For $i = 1, 2, 3$ the experiment gathered the image set S_i corresponding to a particular hopper leg gait G_i .

Table 3 displays the average forward velocity of the robot per leg gait G_i on each terrain tested. It should be

noted that the robot operated at a greater speed on the grass terrain when compared to the velocities seen on the three other tested terrain types. The compliant nature of the grass used in this experiment may have advantageously tuned the hopper's effective leg stiffness. Related research has shown that tuning leg stiffness on a running type robot can significantly alter locomotion performance [46]. The variant forward velocities between terrains, shown in table 3, underscores the importance of a robot knowing the terrain so that the leg gait parameters can be adjusted accordingly.

The multiple images per terrain type and per leg gait recorded with PreSRS were randomly allocated into three data sets, S_1 , S_2 , and S_3 , where $i = 1, 2, 3$ corresponds to hopper leg gait G_i . From table 4, over 300 pressure images I were collected using each leg gait G_i for a total of 961 images.

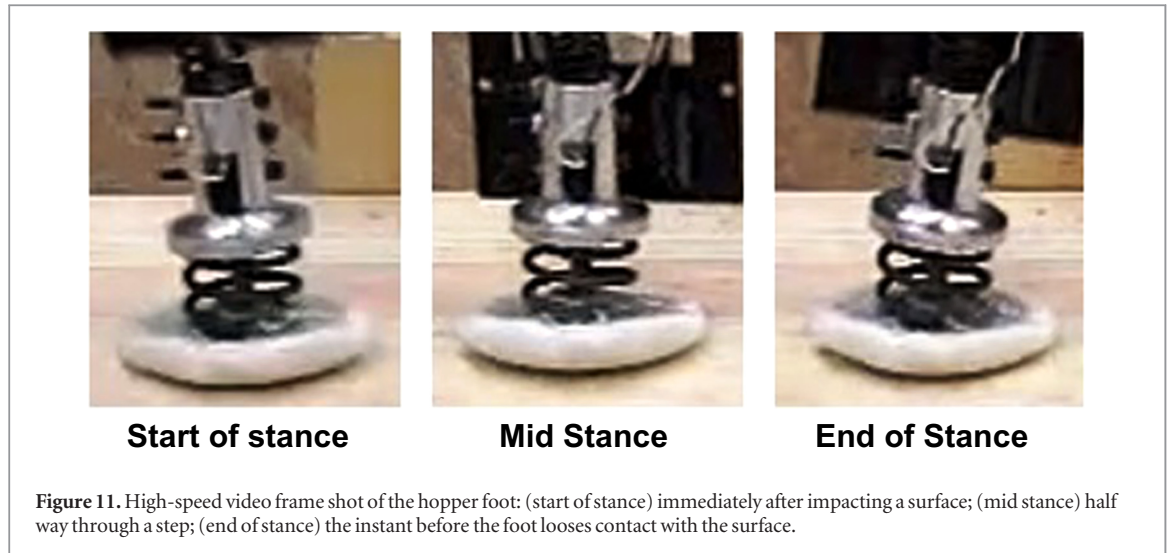
The Evolution[®] acquisition device, displayed in figure 1, samples data from the sensing array at 100 Hz. The stance time (i.e., the amount of time the hopper keeps contact with a surface) is approximately 140 msec, and is the same for each leg gait G_i . Consequently, 14 pressure images can be captured with each robot step. The sub sequential terrain classification described in this section was performed using a single pressure image. These images are extracted at approximately the half-way point a hopper step (e.g., the seventh sampled measurement, and/or 0.07 sec into the stance phase).

Additional classification experiments were performed, implementing pressure images extracted from stance at times: 40 msec, 50 msec, 60 msec, 80 msec, 90 msec, and 100 msec. In each case, the observed accuracy of a trained PWE classifier was similar to using a temporary centralized sample, which will now be discussed.

The bottom three rows and first six columns of image sets S_1 , S_2 , and S_3 were cropped to match the PreSRS foot dimensions of 48.3 mm \times 52.1 mm or 38 pixels \times 41 pixels. There are 1558 individual sensors.

Examples pressure images for each terrain type, taken when the robot was operating at leg gait G_2 , are shown in the second column of figure 12. As can be observed in figure 12, the pressure images are visually (e.g., spatially) distinguishable, suggesting an accurate PWE classifier can be developed using this data.

Feature vectors F_1 , F_2 , and $F_3 \in \mathbb{R}^n$, where $n = 1025$, are computed from the cropped terrain pressure images of the respective sets S_1 , S_2 , and S_3 , following the same protocol outlined in section 4. Example magnitude frequency responses (i.e., feature vectors F_i) on each tested surface type are shown in figure 13. As with the static feature vectors of figure 5, magnitude spikes occur at the same frequencies per terrain type, however with variant magnitudes.

**Table 3.** Gaits.

Gait	Average velocities (m sec ⁻¹)			
	Wood	Carpet	Clay	Grass
G_1	0.40	0.43	0.38	0.81
G_2	0.64	0.63	0.61	1.11
G_3	0.99	0.97	0.84	1.49

Table 4. Number of terrain samples collected on the robot.

Gait	Terrain Type				Total
	Wood	Carpet	Clay	Grass	
G_1	72	43	119	69	302
G_2	60	65	113	85	323
G_3	71	76	102	86	335
Overall	203	184	334	240	961

The plots in figure 13 seem to contain just one feature vector signature; in fact there are three separate feature signatures per plot, each from the sets F_1 , F_2 , and F_3 , respectively. These plots show that a terrain magnitude frequency domain does not vary as robot dynamics vary (e.g. different leg gaits). For this reason, the plots in figure 13 seem to contain just one feature signature each. This observation indicates PreSRS terrain measurements are consistent per sample taken with respect to terrain type, and are not influenced by the robot dynamics.

7.2. Classification

Three separate PWE classifiers C_1 , C_2 , and C_3 , where each correspond to the robot leg gait with matching index. The classifiers were trained using 20 randomly selected feature vectors per terrain type (80 total), and by following the classification methodology outlined in section 4. Training each PWE classifier C_i

constructs two data sets, an unique transformation matrix U and matrix P of reduced order feature dimensionality.

The surface classification accuracies achieved using PreSRS with the one-legged robot are displayed in table 5. For $i = 1, 2, 3$, each trained PWE classifier C_i was used to identify a feature vector $F \notin P$. Columns of table 5 contain the overall classification accuracies (average of the diagonal confusion matrix elements), for each classifier C_i , when identifying the feature vectors $F \notin P$ from leg gait G_j .

Each PWE classifier C_1 , C_2 , and C_3 identified the terrain pressure images captured on all three tested leg gaits with accuracies over 96% (the highest accuracy being 99.3%). The last row in table 5 displays the average classification accuracy of each PWE classifier (i.e., the accuracy of identifying 861 terrain pressure images). The classifier C_2 trained at leg gait G_2 attained the highest overall accuracy of 99.0%.

The findings and observations made in this experiment imply a PWE classifier trained with PreSRS attained pressure images from any leg gait G_i , can produce near perfect accuracies when identifying terrains from any other leg gait G_j , where $i \neq j$. Hence, the PreSRS terrain sensing methodology has the desired quality of capturing terrain signatures that are uninfluenced by the robot dynamics.

Although not detailed in the paper, additional experiments have shown that the classification procedure is also load independent. In particular, the effects of a change in load from that used for training can be accommodated by simply using a scaling factor to adjust the image intensity.

8. Sensor damage

The previous sections have demonstrated PreSRS achieving high terrain classification accuracies over a range of surfaces, using both static and dynamic pressure measurements. This section discusses how

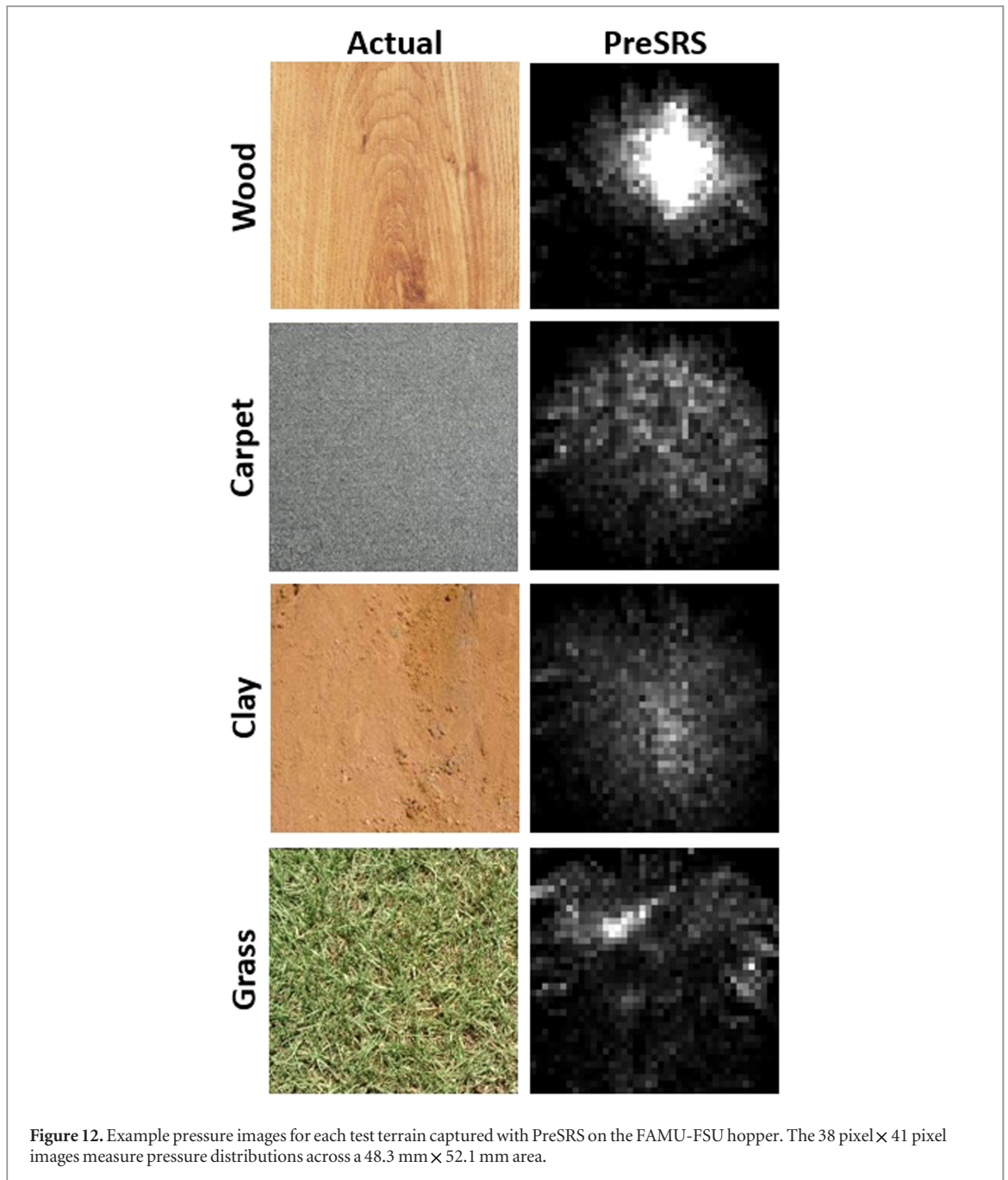


Figure 12. Example pressure images for each test terrain captured with PreSRS on the FAMU-FSU hopper. The 38 pixel \times 41 pixel images measure pressure distributions across a 48.3 mm \times 52.1 mm area.

classification accuracy can vary with sensor damage, a key obstacle associated with using high-resolution pressure sensing arrays. Sensor damage can occur by means of tearing or puncturing the thin (>0.1 mm) polyester sensor material, or through circuitry fatigue associated with loading and unloading the sensor over time.

Each one of the terrain classification experiments presented in this paper was conducted using a new, unused sensing array. PreSRS encountered minor sensor damage when collecting terrain data on the FAMU-FSU hopper, in the experiments of section 7. The damage was minimal and had little to no effect on the classification accuracy.

During robot locomotion, PreSRS was subjected to large impact forces, up to 200 N (approximately $10 \times$ the robot weight). The hard silicon-rubber outer layer protected the sensor from puncture damage, even on extreme terrains such as gravel, one of the surfaces tested in section 4. The inner compliant layers comprising the majority of PreSRS as shown in figure 1, dampens a portion of this impacting force. However over repeated steps, even on benign terrains, the sensing array will inevitably suffer from circuitry fatigue damage. Damage tears a single conductive horizontal or vertical circuit trace (i.e., row or column). The result is an open circuit that can no longer measure forces along the torn trace. The acquisition

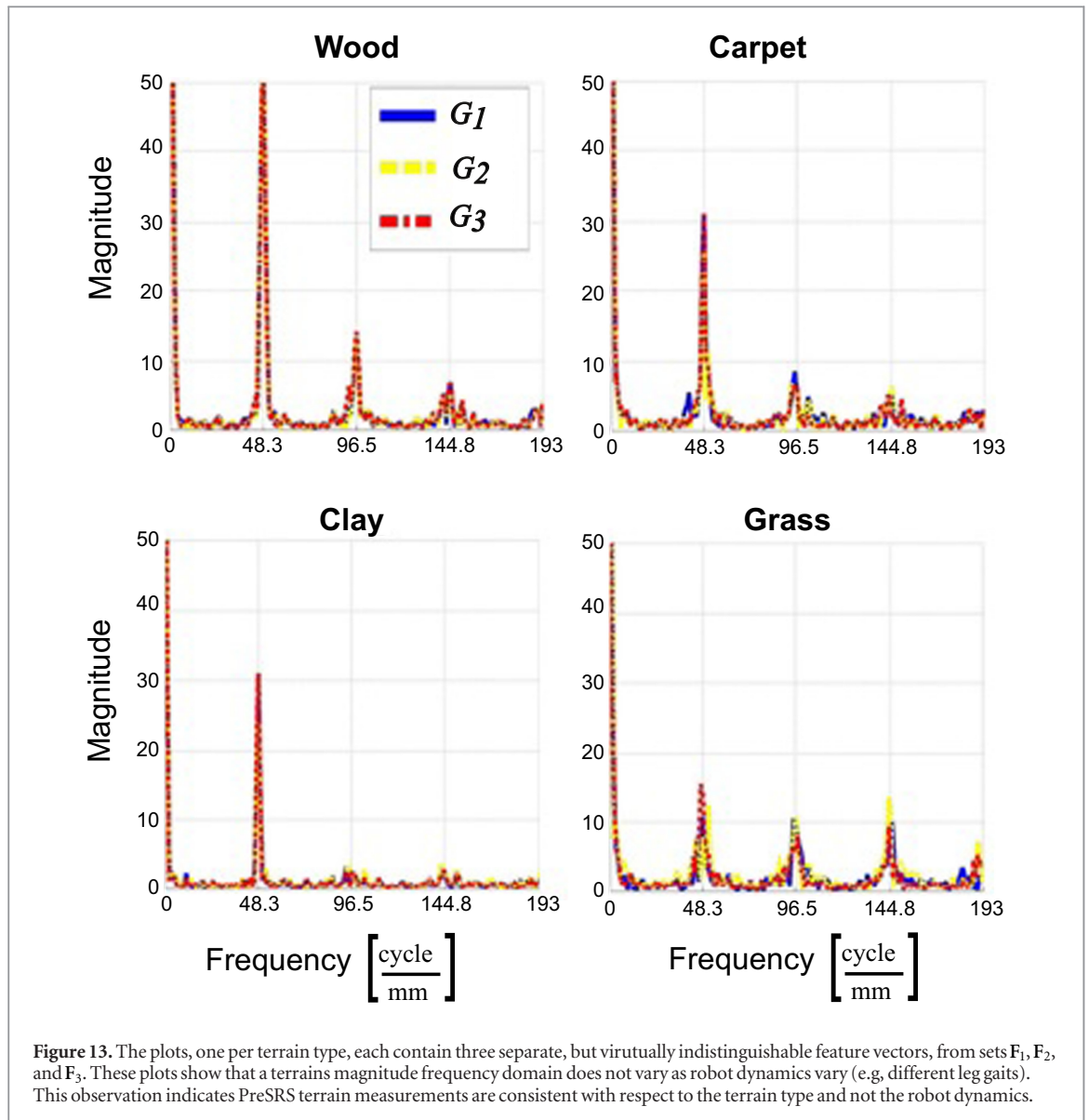


Table 5. Dynamic results.

Terrain classification accuracies			
Tested gait	Trained classifier		
	C_1	C_2	C_3
G_1	97.6%	99.3%	97.8%
G_2	96.8%	99.1%	96.8%
G_3	96.5%	98.6%	98.3%
Overall	96.3%	99.0%	97.6%

software defaults the malfunctioning grid row or column with zero values.

961 pressure images were collected with PreSRS for the dynamic terrain classification experiment described in section 7. The damage done on the sensor during the dynamic experiment was one damaged row and two damaged columns. Recalling the pressure images were cropped to 38 pixel \times 41 pixel images,

sensor damage from the experiment can be approximated at 7% using

$$\text{Damage} = \frac{d_r n_c + d_c n_r - d_r d_c}{n_r n_c} \times 100\%, \quad (6)$$

where n_r and n_c depict the total number of rows and columns making up the sensing grid, and d_r and d_c represent the number of damaged rows and columns, respectively.

Using the captured pressure images and the trained PWE classifier C_2 from section 7, an experiment was performed to determine the relationship between classification accuracy and sensor damage. Only the pressure images not used to train the PWE classifier C_2 were used in the experiment (861 samples total). Sensor damage was simulated by creating the damaged image sets D_1 , D_2 , ..., D_{75} . Each image set contained pressure images progressively influenced with more damage, which is done by randomly

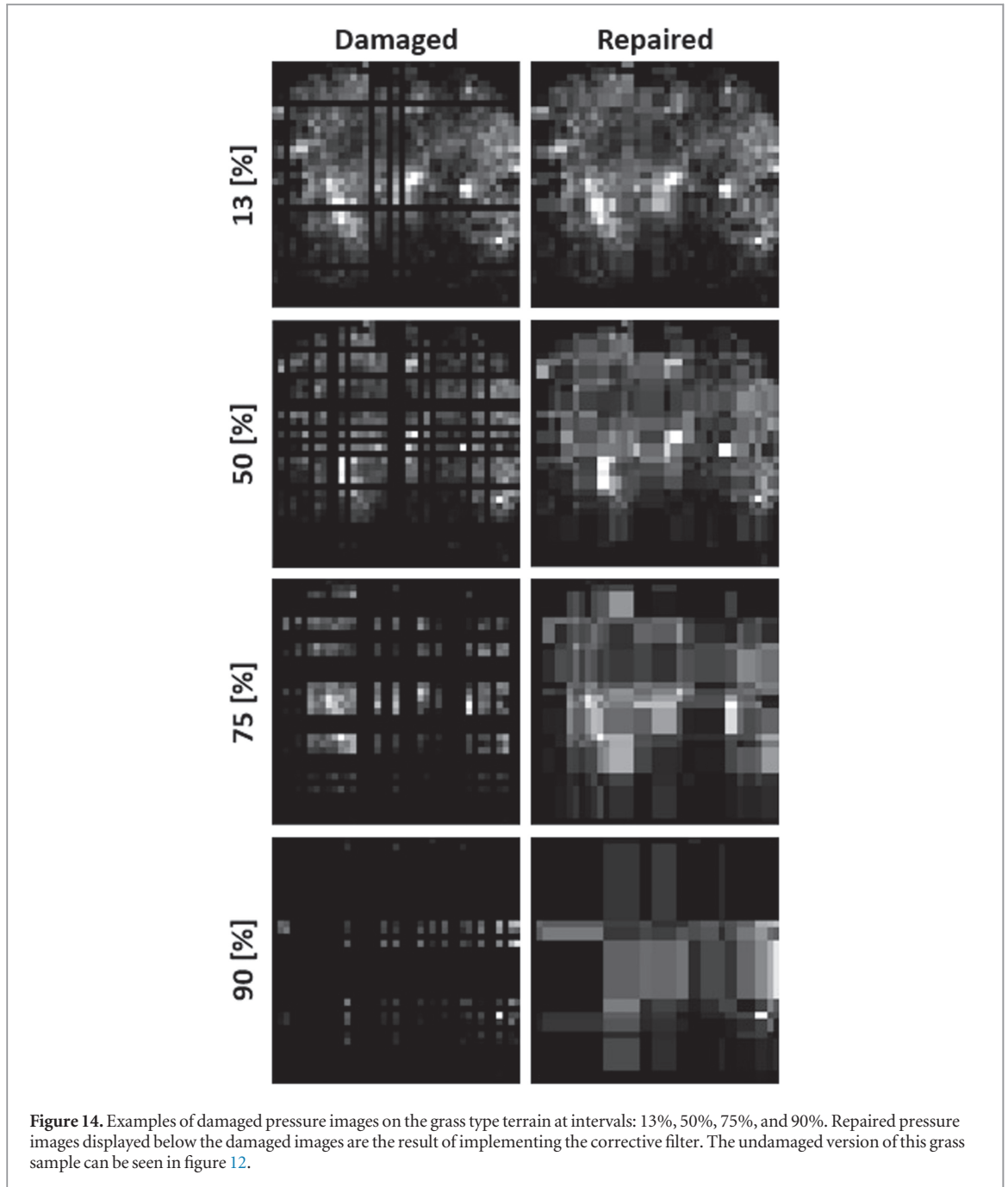


Table 6. Loss of classification accuracy (>90%): average metrics.

Metric	Without repair	With repair
Min	7.52	54.7
Km	0.352	2.56
Improvement factor: 6.27		

deactivating (set to zero) image rows and columns. The images in set D_1 contained one damaged row or column, and the images in D_{75} were damaged 100%.

Figure 14 displays examples of damaged pressure images at increments: 13%, 50%, 75%, and 90% on

the grass terrain type; the undamaged image can be seen in figure 12. At 90% damage, a sample pressure image contains only 154 active sensors out of 1558 available sensors.

The relationship between terrain classification accuracy and sensor damage was determined by identifying each damaged image set D_i with the trained PWE classifier C_2 , which was formulated in section 7. The dashed curve shown in figure 16 depicts this relationship, where the x -axis spans the sensor damage percent, and the y -axis spans the classification accuracy. Any accuracy above 90% is considered acceptable. This determination was based upon the near

perfect accuracies demonstrated in sections 4 and 7. From figure 16 the accuracy drops below 90% with approximately 13% sensor damage.

Three performance metrics can be calculated from the robot gait velocity and step number data from tables 3 and 6. These metrics estimate the percent of damage inflicted on PreSRS per Hopper step, per minute of operation, and per kilometer of forward travel. The expected PreSRS life-span on the FAMU-FSU hopper (i.e., the point when the classification accuracy falls below 90%) is approximately 7.52 min of operation, or 0.352 km of forward travel. The expected life-span of PreSRS for this prototype is not long.

The short operating life expectancy indicates PreSRS is not yet a viable system for application on field-ready robots. In order to increase PreSRS performance over time, improved mechanical robustness and/or signal processing is required. The research presented here, investigated a signal processing solution to enable high classification accuracy in the presence of sensor damage.

First, image repair was attempted using standard image corrective filtering techniques such as image convolution, statistical pixel windows, and pixel interpolation [47]. Using these filters increased the amount of damage PreSRS can sustain to about 25% before classification dropped below acceptable accuracies.

The effect sensor damage has on the magnitude frequency response can be seen in the left column of figure 15. The spike frequencies match between damaged and undamaged signals, but the magnitudes diminish with increasing sensor damage, which is the reason PreSRS accuracy drops below 90% with 13% sensor damage. These observations led to the development of an unconventional image filtering technique, one designed to return image intensity to the undamaged likeness. By accomplishing this, the magnitude spikes in the frequency domain are preserved in the presence of sensor damage.

Undamaged image spatial intensity is restored with this new image filter by first scanning for damaged rows (top to bottom) in the image. Once detected, all the elements in the row are replaced with the previous (either undamaged, or recently repaired) row values. Once the rows are repaired, the filter corrects the columns (left to right) in the same manner as the rows. Repaired image sets are designated as R_1 , R_2 , and R_3 .

This technique of replacing damaged (zero value) pixels with neighboring undamaged pixel values returns the original image intensity, whereas standard image repairing techniques such as statistical pixel windows, and pixel interpolation [47], tend to diminish the intensity. The repairing filter only alters the damaged pixels in an image and not the undamaged pixels. This repairing technique was meant to be used with the types of images captured with PreSRS, and may not work with other image types (e.g., digital photographs).

The right hand column in figure 14 displays the repaired pressure images resulting from applying the new corrective filter on the damaged grass images. The filter does not visually correct the image spatial domain likeness. Instead the filter fixes the image frequency domain. In particular, as illustrated in the right hand column of figure 15, the magnitude frequency spikes of both the repaired and undamaged feature vectors are closely matched, even at 90% sensor damage.

Repaired image sets R_i were classified using the PWE classifier C_2 trained in section 7. The solid line in figure 16 shows the PreSRS classification accuracies obtained from each set. PreSRS accuracy remains around 97% until suffering approximately 80% damage. At this point the classification accuracy decreases, and at 90% sensor damage PreSRS accuracy falls below the acceptable 90% accuracy range. Hence, the repairing filter enables PreSRS to achieve accuracies above 90%, even at 90% sensor damage, where only 152 of 1558 individual pressure sensors are functioning on the sensing grid.

Table 6 compares PreSRS operational limits when the repairing filter was used and when it was not used on damaged terrain pressure images. From the performance metrics, PreSRS can now classify terrains accurately for approximately 53 min, or 2.50 km of forward travel. Hence, the developed image repairing filter extends PreSRS life-span by a factor of 6.27 when compared to using no filter.

These results suggest an advantage of using a high-resolution sensing array for robot skins. High-resolution sensing provides redundant terrain information (i.e., the many pixels in the pressure image), which can be used by the repairing filter to ‘fill in’ lost pressure sensor measurements in the event of sensor damage.

High terrain accuracies can be attained (above 96% on distinct terrain types as in section 5) with a similar but lower-resolution sensing arrays that can generate images with as few as 10 pixels \times 10 pixels. However, high-resolution sensors constructed in the same manner should have a much higher life-span, due in part to their numerous sensors, in spite of fatigue damage that inevitably occurs.

9. Conclusions

This paper describes the development and demonstration of a proprioceptive approach to surface classification that relies on distributed pressure measurements from an artificial skin. Human skin was used as a template in the construction of the PreSRS.

The dermis (middle) layer consisted of a high-resolution pressure sensing array, which has a pressure sensor density similar to that in human skin. An appropriate compliant material emulated the subcutaneous (inner) and epidermis (outer) layers of a human skin. These layers enable the pressure sensors

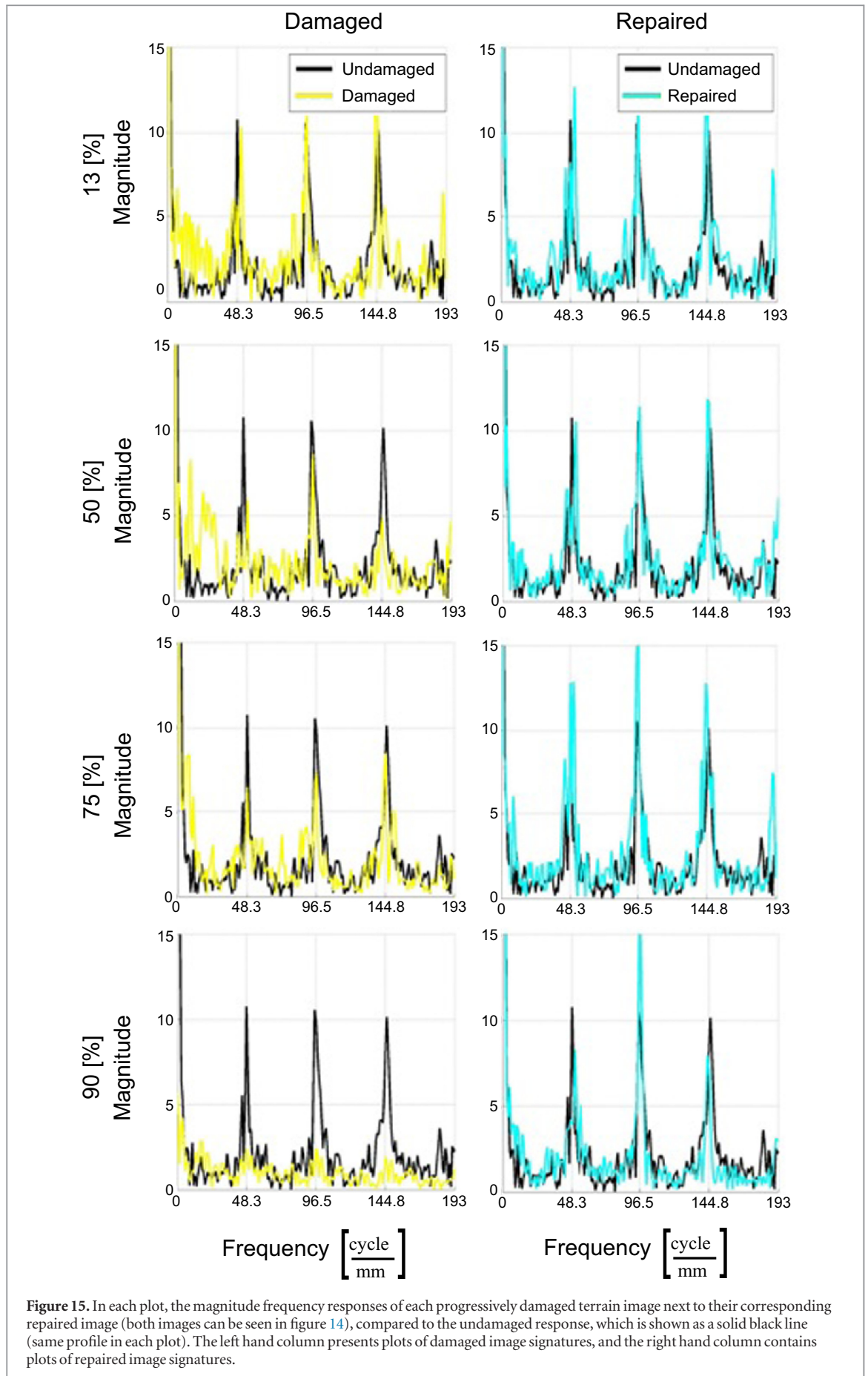
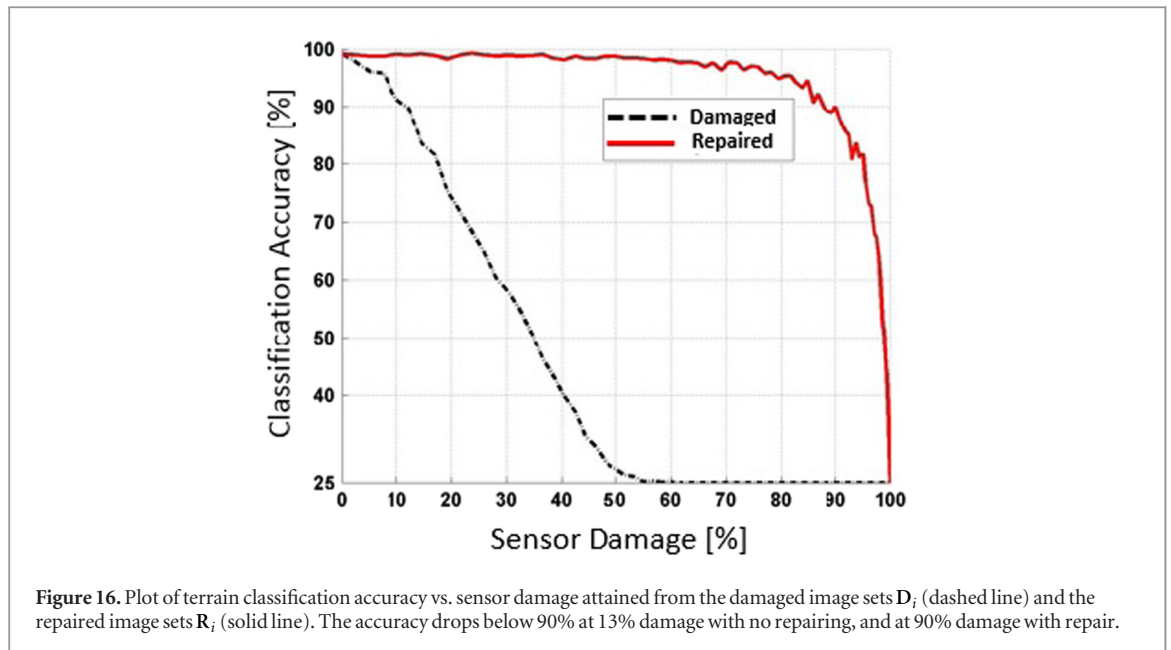


Figure 15. In each plot, the magnitude frequency responses of each progressively damaged terrain image next to their corresponding repaired image (both images can be seen in figure 14), compared to the undamaged response, which is shown as a solid black line (same profile in each plot). The left hand column presents plots of damaged image signatures, and the right hand column contains plots of repaired image signatures.



in the dermis layer to have maximal contact with the surface that the skin contacts. A felt type fabric was used as the compliant material in PreSRS, while an outer layer of hard silicon-rubber was used as the outermost element of the epidermis to protect PreSRS against puncturing or tearing.

In this research PreSRS was used to generate the pressure images upon which the surface classification was based. However, the classification approach will apply to any robot skin that has uniformly spaced pressure measurements. The surface classification approach is based on the observation that the magnitude of the spatial frequency response of a surface constitutes a terrain signature. PCA was used to reduce the feature vector dimensions to achieve fast classification times. The classifier used in this research was a PWE.

The first insight from static (stationary) terrain classification experiments was that a high-resolution sensor (40 sensor \times 40 sensor grid) allows for high accuracy identification of both dissimilar surfaces (99.7% overall accuracy) as well as between fine granulations of sandpaper (96.7% overall accuracy). Reduction of the sensor image to a 10 sensor \times 10 sensor grid preserved the high classification accuracy attained on dissimilar terrains (96.6% overall accuracy), but not on similar terrains i.e., sandpaper (58.0% overall accuracy). While the low-resolution approach is accurate, high-resolution sensing is necessary to enable a robot to enable the distinction of terrains that tend to feel similar to even human touch.

Surface classification with PreSRS was extended to dynamic classification using the FAMU-FSU hopper as a test bed. This research developed a foot concept based on human ankle biology, which enabled the robot skin to have maximal contact with the terrain surface during the stance phases of motion. Dynamically measured pressure images were implemented for

classification purposes by extracting a sample at a fixed stance time, i.e., the time after the foot initially impacts the ground. This proved to be highly effective.

A primary goal of this research was to develop a gait and payload independent terrain classification methodology. Since, a robot skin takes measurements through direct contact with a surface, it should capture terrain signatures unaffected by the robot's dynamics and hence the robot's operating condition (e.g., gait or payload). Gait-independent terrain classification was tested using the FAMU-FSU hopper operating on four distinct terrains under three leg gaits G_1 , G_2 , and G_3 of increasing velocity. A PWE classifier was trained with pressure images taken only while the robot was moving in the intermediate gait G_2 . The classifier achieved a near perfect overall accuracy of 99.0% when identifying pressure images from each tested leg gait G_1 , G_2 , and G_3 . This result tremendously simplifies the training process in comparison to existing proprioceptive approaches since the classifier requires terrain measurements from only one operating condition, instead of many.

Although the thin (>0.1 mm) polyester sensor in PreSRS was protected against puncture and tearing damage, it was found that the sensor exhibits fatigue damage from repeated impacts with the surface. This fatigue damage dramatically affected the overall terrain classification accuracies of PreSRS. Restoring the pressure image intensity via an innovative image repairing filter is a key contribution of this research. This filter enables PreSRS to achieve accuracies above 90% even when the sensing array is 90% damaged, dramatically increasing the classification life of PreSRS. The pressure image repairing filter relied on the high resolution of the pressure images, providing a second reason for using high-resolution pressure images.

Research in this area can proceed in several directions. First, there is the fundamental problem of developing robot skins that are robust with respect to fatigue damage. This can be accomplished, for example, by developing more rugged pressure sensor arrays (e.g., capacitance based arrays should be investigated) or using compliant layers and an outer protective layer that provide more protection than the materials used in this research.

Additionally, this approach can be applied to help the end effectors of robot manipulators sense surfaces. Pressure sensing is only one sensing modality as vibration-based approaches have already proven to be effective for surface classification. Combining the various sensing modalities including vision, temperature, and moisture sensing, is an important research direction. This research should ultimately determine how to use the various sensing methods synergistically or determine when one is more reliable than another.

In the future, this work will enable autonomous running robots to adapt their leg gaits in real-time to changes in the environment, improving speed, stability, and efficiency of running in natural settings and enhancing the accuracy of motion planning. The findings of this paper strongly suggest surface identification via PreSRS can be extended to autonomous field robots, providing the robot with crucial information about the environment that can be used to aid stable and efficient mobility over rough and varying terrains.

Acknowledgments

This work was supported by the US Army Research Laboratory under the Robotics Collaborative Technology Alliance program, Cooperative Agreement W91NF-0-2-006.

References

- [1] Raibert J and Marc H 1986 *Legged Robots That Balance* (Cambridge, MA, USA: Massachusetts Institute of Technology)
- [2] Saranli U, Buehler M and Koditschek D E 2001 RHex: a simple and highly mobile hexapod robot *Int. J. Robot. Res.* **20** 616–31
- [3] Galloway K and Clark J E 2013 Variable stiffness legs for robust, efficient, and stable dynamic running *J. Mech. Robot.* doi:10.1115/1.4007843
- [4] Miller B, Andrews B and Clark J 2010 Improved stability of running over unknown rough terrain via prescribed energy removal *12th Int. Symp. on Experimental Robotics*
- [5] Asif U and Iqbal J 2011 An approach to stable walking over uneven terrain using a reflex-based adaptive gait *J. Control Sci. Eng.* **2011** 12
- [6] Revzen S and Ilhan B 2012 Dynamical trajectory replanning for uncertain environments *IEEE 51st Annual Conf. on Decision and Control (CDC) (Maui, Hawaii, USA, December 2012)*
- [7] Manjanna S, Dudek G and Giguere P 2013 Using gait change for terrain sensing by robots *Proc. Int. Conf. on Computer and Robot Vision (May 2013)* (Los Alamitos, CA: IEEE Computer Society Press) 16–22
- [8] Ferris D P, Liang K and Farley C T 1999 Runners adjust leg stiffness for their first step on a new running surface *J. Biomech.* **32** 787–94
- [9] Fong D T-P, Hong Y and Li J-X 2009 Human walks carefully when the ground dynamic coefficient of friction drops below 0.41 *Saf. Sci.* **47** 1429–33
- [10] Moghadam P and Wijesoma W 2009 Online, self-supervised vision-based terrain classification in unstructured environments *Proc. IEEE Conf. on Systems, Man and Cybernetics* **11** 3100–5
- [11] Rankin A L and Matthias L H 2008 Mud detection for unmanned ground vehicle autonomous navigation *Proc. 26th Army Science Conf.*
- [12] Andersen J C, Blas M R, Ravn O, Andersen N A and Blanke M 2006 Traversable terrain classification for outdoor autonomous robots using single 2d laser scans *Integr. Comput.-Aided Eng.* **13** 223–32
- [13] Mertz C, Kozar J, Miller J R and Thorpe C 2001 Eye-safe laser line striper for outside use *Proc. IEEE Conf. on Intelligent Vehicle Symp.*
- [14] Lu L, Ordonez C, Collins E, Coyle E and Palejiya D 2011 Terrain surface classification with control mode update rule using a 2d laser stripe-based structured light sensor *Robot. Auton. Syst.* **59** 954–65
- [15] Coyle E, Collins E, DuPont E, Dang D, Wang H, Cooper R and Grindle G 2008 Vibration-based terrain classification for electric powered wheelchairs *Proc. 4th IASTED Int. Conf. on Telehealth and Assistive Technologies (Baltimore, MD, 16–18 April 2008)* 139–44
- [16] Ward C C and Iagnemma K 2008 Speed-independent vibration-based terrain classification for passenger vehicles *Veh. Syst. Dyn.* **47** 1–19
- [17] Dupont E, Collins E, Coyle E and Roberts R 2010 Terrain classification using vibration sensors: theory and methods *Mobile Robots: New Research* (Hauppauge, NY: Nova Science)
- [18] Giguere P, Dudek G, Prahacs C and Saunderson S 2011 Environment identification for a running robot using inertial and actuator cues *Proc. IEEE Conf. on Robotics and Automation (Montreal, Canada)*
- [19] Ordonez C, Shill J, Johnsons A, Clark J and Collins E 2013 Terrain identification for RHex-type robots *Proc. SPIE Defense Security, and Sensing Conf. (Baltimore, MD, 29 April–3 May 2013)*
- [20] DuPont E, Moore C, Collins E and Coyle E 2008 Frequency response method for online terrain identification in unmanned ground vehicles *Auton. Robots* **24** 337–47
- [21] Hillis W D 1982 A high-resolution imaging touch sensor *Int. J. Robot. Res.* **1** 33–44
- [22] Dyson C, Yauilla N and Kolesar E S 1993 Object imaging with a piezoelectric robotic tactile sensor *Proc. IEEE National Aerospace and Electronics Conf. (May 1993)* **1** 41–47
- [23] Pezzementi Z, Plaku E, Reyda C and Hager G D 2011 Tactile-object recognition from appearance information *Proc. IEEE Conf. on Robotics and Automation* **27** 473–87
- [24] Sinapov J, Sukhoy V, Sahai R and Stoytchev A 2011 Vibrotactile recognition and categorization of surfaces by a humanoid robot *Proc. IEEE Conf. on Robotics and Automation* **27** 488–97
- [25] Fishel J A and Loeb G E 2012 Bayesian exploration for intelligent identification of textures *Frontiers Neurobot.* **6** 1–20
- [26] PPS. 2013 Pressure profile systems. Pressure Profile Systems Inc. Los Angeles, CA (available: <http://www.pressureprofile.com>)
- [27] Liu Y-H, Hsiao Y-T, Cheng W-T, Liu Y-C and Su J-Y 2014 Low-resolution tactile image recognition for automated robotic assembly using kernel pca-based feature fusion and multiple kernel learning-based support vector machine *Math. Probl. Eng.* **2014** 11
- [28] Sinapov J, Bergquist T, Schenck C, Ohiri U, Griffith S and Stoytchev A 2011 Interactive object recognition using proprioceptive and auditory feedback *Int. J. Robot. Res.* **30** 1250–62

- [29] Su Z, Fishel J, Yamamoto T and Loeb G 2012 Use of tactile feedback to control exploratory movements to characterize object compliance *Frontiers Neurobot.* **6** 1–9
- [30] Thonnard J L and Bleyenheuft Y 2009 Development of touch *Scholarpedia* **4** 58–79
- [31] Vallbo A B and Johansson R S 1984 Properties of cutaneous mechanoreceptors in the human hand related to touch sensation *Hum. Neurobiol.* **3** 3–14
- [32] Mechanoreceptors specialized to receive tactile information Purves D, Augustine G, Fitzpatrick D et al (ed) 2001 *Neuroscience* 2nd edn (Sunderland, MA: Sinauer)
- [33] TekScan. (2013) Sensor map #5051. 307 West First Street. South Boston, MA 02127-1309, USA (available: <http://www.tekscan.com/5051-pressure-sensor>)
- [34] Shill J J, Collins E G, Coyle E and Clark J 2014 Terrain identification on a one-legged hopping robot using high-resolution pressure images *IEEE Inter. Conf. Robotics and Automation (ICRA) (May-June 2014)*
- [35] Pereira J, Mansour J and Davis B 1991 Dynamic measurement of the viscoelastic properties of skin *J. Biomech.* **24** 157–62
- [36] Liang X and Boppart S A 2010 Biomechanical properties of in vivo human skin from dynamic optical coherence elastography *IEEE Trans. Biomed. Eng.* **57** 953–9
- [37] Schaefer R 2002 *Harris' Shock and Vibration Handbook* 5th edn (New York: McGraw-Hill) pp 33–51
- [38] Aqua-Calc. (2005-2013) Aqua-calc: Density measurements (available: <http://www.aqua-calc.com/page/density-table/substance>)
- [39] Lee M and Nicholls H 1999 Review article tactile sensing for mechatronics—a state of the art survey *Mechatronics* **9** 1–31
- [40] Collins E and Coyle E 2008 Vibration-based terrain classification using surface profile input frequency responses *Proc. IEEE Conf. on Robotics and Automation (Pasadena, CA, 19–23 May 2008)* 3276–83
- [41] Coyle E and Collins E 2008 A comparison of classifier performance for vibration-based terrain classification *26th Army Science Conf. (Orlando, FL, 1–4 December 2008)*
- [42] TekScFederation. (2012) Fepa-standard 42-1:2006. 64283 Darmstadt, Germany (available: <http://www.fepa-abrasives.org>)
- [43] Andrews B, Miller B, Schmitt J and Clark J 2011 Running over unknown rough terrain with a one-legged planar robot *Bioinspiration Biomimetics* **6** 1–15
- [44] Kolger G and Shorten M 2001 Plantar pressure distribution during gait in a subject without adipose tissue in the heel and ball of the foot *Proc. 5th Symp. on Footwear Biomechanics (December 2001)*
- [45] Elftman H 1969 Dynamic structure of the human foot *Artificial Limbs* **13** 49–58
- [46] Galloway K, Clark J, Yim M and Koditschek D 2011 Experimental investigations into role of passive variable compliant legs for dynamic robotic locomotion *IEEE Int. Conf. on Robotics and Automation (May 2011)*
- [47] Gonzalez R and Woods R E 2002 *Digital Image Processing* (Englewood Cliffs, NJ: Prentice Hall)

QUERY FORM

JOURNAL: Bioinspiration & Biomimetics

AUTHOR: JJ Shill *et al*

TITLE: Tactile surface classification for limbed robots using a pressure sensitive robot skin

ARTICLE ID: bb502353

The layout of this article has not yet been finalized. Therefore this proof may contain columns that are not fully balanced/matched or overlapping text in inline equations; these issues will be resolved once the final corrections have been incorporated.

Page 1

Q1

We have been provided funding information for this article as below. Please confirm whether this information is correct. Robotics Collaborative Technology Alliance program, Cooperative Agreement: W91NF-0-2-006.
